Flexural contact in MEMS stiction

Yin Zhang *, Ya-pu Zhao

State Key Laboratory of Nonlinear Mechanics, Institute of Mechanics, Chinese Academy of Sciences, Beijing 100190, China

ABSTRACT

Adhesive force between two solid surfaces can lead to stiction failure of the micro-electro-mechanical systems (MEMS) device. The competition between the adhesive force and the beam restoring force determines whether the stiction occurs or not. Previous models assume that the stuck beam deforms either as the arc-shape or the S-shape, which causes significant differences in the measurements of adhesion and disputations among researchers. The contact mechanics model presented in this paper shows that the assumptions of the arc-shape and S-shape on the beam deformation over-simplify the problem; both the arc-shaped deformation and S-shaped deformation significantly deviate from the real ones. The previous theories are shown to be incompatible with the recent experimental results. The model presented in this paper attempts to explain those new experimental results and resolve some disputations on the previous models. The instabilities of jump-in during loading process and jump-off during unloading process are also incorporated in this model.

© 2012 Elsevier Ltd. All rights reserved.

1. Introduction

Stiction is a major failure mechanism for MEMS structures (Legtenberg et al., 1994; Mastrangelo and Hsu, 1993a,b). Stiction occurs in a two-step process (Legtenberg et al., 1994): Firstly, an external load such as capillary force (Legtenberg et al., 1994), electrostatic force (de Boer and Michalske, 1999), mechanical load (Jones et al., 2003a,b) and inertial forces (shock, rapid flows) (de Boer and Michalske, 1999), brings the suspended MEMS structure into contact with a substrate. Secondly, once the contact is initiated, an attachment state called stiction can be formed even after the external load is retracted. For the first step, the physical picture is rather clear. For example, if the external load is capillary force, the capillary force per unit length, q, is (Legtenberg et al., 1994; Mastrangelo and Hsu, 1993a)

$$q = \frac{2B\gamma_l(\cos\theta_1 + \cos\theta_2)}{H - W(x)} \tag{1}$$

As shown in Fig. 1, $2B$ and $W(x)$ are the MEMS beam width and deflection, respectively; H is the gap distance between the undeformed beam and substrate; γ_l is the surface tension of the liquid; θ_1, θ_2 are the contact angles of liquid/beam and liquid/substrate. The capillary force varies nonlinearly with W as indicated by Eq. (1); the restoring force varies linearly with a spring stiffness proportional to $E_1I/(2L)^3$ (Legtenberg et al., 1994). E_1, I and $2L$ are the beam Young's modulus, the area moment of inertia and length,

respectively. There is a critical point at which the restoring force can no longer balance the capillary force: the beam has an abrupt jump into contact with substrate (Mastrangelo and Hsu, 1993a), which is called pull-in (Legtenberg et al., 1994) or jump-in (Yang, 2004). Mastrangelo and Hsu (1993a) defined a dimensionless parameter called elastocapillary number N_{EC}, which in essence indicates the ratio of the maximum elastic energy to the maximum capillary energy. $N_{EC} < 1$, the contact between the MEMS structure and substrate occurs; $N_{EC} > 1$, there is no contact. Similarly, Legtenberg et al. (1994) defined a critical length called pull-in length, L_{PI}, as

$$L_{PI} = 1.059\left[\frac{8E_1H^2T^3}{\gamma_l(\cos\theta_1 + \cos\theta_2)}\right]^{1/4} \tag{2}$$

T is the beam thickness. γ_l, θ_1 and θ_2 are the fixed values for a given liquid. Therefore, for given H and T, if a clamped–clamped beam length is larger than this L_{PI}, the beam contacts the substrate; otherwise, there is no contact. Based on the theories by Mastrangelo and Hsu (1993a) and Legtenberg et al. (1994), the abrupt jump of contact is caused by the competition between the nonlinear external force (such as capillary force) and linear elastic restoring force. However, this study reveals that with the presence of adhesion, this abrupt jump behavior is inevitable even for the case of constant external loading.

The debate is on the second step. Once the external load is gone, the solid–solid interfacial/adhesion energy competes with the beam elastic energy due to deformation, which determines whether the stiction occurs or not. The key issue here is on the calculation of the system elastic energy and the problem lies in the boundary conditions at the contact separation points indicated as

* Corresponding author.
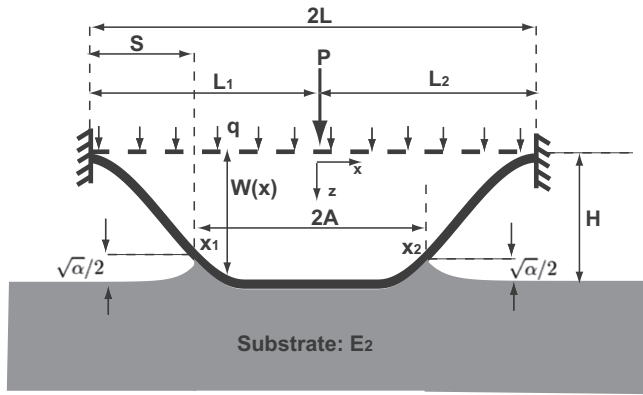 E-mail address: zhangyin@lnm.imech.ac.cn (Y. Zhang).

Fig. 1. Schematic diagram of a C–C beam under a uniformly distributed load and a concentrated load.

x_1 and x_2 in Fig. 1. Two deformation shapes for a stuck beam are found: the arc-shape and S-shape (de Boer and Michalske, 1999; de Boer et al., 1999; Jones et al., 2003a; Rogers et al., 2002). Rogers et al. (2002) presented a summary on the formation of the arc-shape and S-shape: shorter beam forms the arc-shape and its unstuck length is approximately equal to the beam length; longer beam forms the S-shape and its unstuck length is appreciably shorter than the beam length. For the arc-shaped deformation, the boundary conditions at the contact separation point are the hinged ones as shown in Appendix A; for the S-shaped deformation, the boundary conditions at the contact separation point are the clamped ones. The bending moment at a hinged point is zero. The zero bending moment has been used by Timoshenko (1956) and Weitsman (1970) as a boundary/matching condition for a beam contact with a substrate. However, Yang (2004) argued that the bending moment cannot be zero at the contact separation point for an adhesive contact. According to Yang (2004), the boundary conditions at the contact separation point can only be the clamped ones. On the other side, the rotation angle of the S-shape deformation at the contact separation point is zero because of the clamped boundary conditions. However, de Boer and Michalske (1999) found that the rotation angle at the contact separation point is not zero. Furthermore, Gladwell (1976) and Kerr (1976, 1979) showed that the boundary/matching conditions at the separation point(s) are neither the clamped ones nor the hinged ones. Therefore, the first question raised here is: (1) *how are the arc-shaped and S-shaped deformations formed and what are the exact boundary conditions at the contact separation point(s)*?

A critical length L_s related with stiction is defined as follows:

$$L_s^4 = C \frac{E_1 H^2 T^3}{\gamma_s} \tag{3}$$

γ_s is the solid–solid interfacial/adhesion energy between the beam and substrate, which is also known as Dupré work of adhesion (Yu and Suo, 1998; Zhao et al., 2003). C is a constant, $C = 3/8$ for the arc-shaped beam and $C = 3/2$ for the S-shaped beam (de Boer and Michalske, 1999; de Boer et al., 1999; Yang, 2004). Physically, L_s is the critical suspension length (S) as indicated in Fig. 1. L_s can be obtained by calculating the critical energy release rate of a deformed beam via a fracture mechanics approach (de Boer and Michalske, 1999; de Boer et al., 1999; Knapp and de Boer, 2002; Jones et al., 2003a), or by minimizing the system total energy (Mastrangelo and Hsu, 1993b; Yang, 2004). If the cantilever beam length (de Boer and Michalske, 1999; de Boer et al., 1999; Mastrangelo and Hsu, 1993b) or the half length of a clamped–clamped beam (Yang, 2004) exceeds this L_s, stiction occurs; otherwise there is no stiction. L_s is also called the detachment length (Mastrangelo and Hsu,

1993b; Legtenberg et al., 1994; Raccurt et al., 2004), or more directly, the length of the shortest adhered beam (Rogers et al., 2002). Eq. (3) indicates that the beam length has no impact on L_s, which is not true as shown later in this study. Mastrangelo and Hsu (1993b) defined the following dimensionless parameter called the peel number for a cantilever

$$N_P = \frac{3}{8} \frac{E_1 H^2 T^3}{\gamma_s L_s^4} \tag{4}$$

No stiction occurs for $N_P > 1$ and stiction occurs for $N_P < 1$ (Mastrangelo and Hsu, 1993b). From Eq. (3), it is not difficult to tell that the peel number of Eq. (4) is obtained by assuming the arc-shape deformation.

Eq. (3) can be rewritten as the following:

$$\gamma_s = C \frac{E_1 H^2 T^3}{L_s^4} \tag{5}$$

Eq. (5) is used to measure γ_s. In experiments, a beam array with different lengths are put into test (de Boer and Michalske, 1999; Mastrangelo and Hsu, 1993b; Knapp and de Boer, 2002; Rogers et al., 2002). From the experiments, L_s is found from the stuck beam with the shortest length (Knapp and de Boer, 2002; Rogers et al., 2002). Because C depends on whether the beam deforms as the arc-shape or as the S-shape, choosing C as 3/8 (arc-shape) or as 3/2 (S-shape) will cause four times difference on γ_s. From Eq. (3), $L_s^{arc} = \left(\frac{3E_1 H^2 T^3}{8\gamma_s}\right)^{1/4}$ for the arc-shape and $L_s^{S} = \left(\frac{3E_1 H^2 T^3}{2\gamma_s}\right)^{1/4}$ for the S-shape. Because $L_s^{arc} = \frac{\sqrt{2}}{2} L_s^{S}$ is a shorter one, $C = 3/8$ of arc-shape is a natural choice (Mastrangelo and Hsu, 1993b; Raccurt et al., 2004). However, de Boer and Michalske (1999) argued that adhesion of γ_s measured by (assuming) the arc-shape is unreliable; they suggest that only the S-shaped beam configuration should be adopted for the detailed study of adhesion. Now, our second question arises: (2) *what kind of deformation shape should we take for the stiction study*?

Polysilicon is the material often used in the adhesion study. After surface treatment, polysilicon can becomes either hydrophilic (with large γ_s) or hydrophobic (with small γ_s). Table 1 lists some measured data for the adhesion energy of a polysilicon. The huge difference on the measured adhesion energy had been noticed before (Jones et al., 2003a). The surface treatments on the samples of polysilicon and test environment by different groups are different (Jones et al., 2003a), which is directly responsible for the different adhesion energy measurements. Furthermore, the compliance of step-up post (de Boer and Michalske, 1999), surface roughness (Delrio et al., 2005; Hariri et al., 2006; Tas et al., 2003), humidity of testing environment (de Boer et al., 1999), defects of coating film (de Boer et al., 1999), plastic deformation (Jones et al., 2003a,Tas et al., 2003; van Spengen et al., 2002), thermal stress (Rogers et al., 2002) and residual strain/stress (Legtenberg et al., 1994; Wong et al., 2007) etc. can all be the factors causing different measurements, which are not embodied in Eq. (5). Hariri et al. (2006) commented that "the inconsistency and unreliability of the experimental data" are the main deficiencies of those experiments; some of data are even observed to be in contradiction with one another. More explicitly, van Spengen et al. (2002) concluded that "the surface interaction energy measurement using stuck beams needs considerable research before we can conclude anything definite about the precise magnitude of the measured surface interaction energy". A key issue related with the above two questions is that the elastic energy inside the contact zone is not accounted by either the energy approach (Mastrangelo and Hsu, 1993b; Legtenberg et al., 1994; Yang, 2004) or the fracture mechanics approach (de Boer and Michalske, 1999; Jones et al., 2003a; Knapp and de Boer, 2002; Leseman et al., 2007). This

Table 1
Measured adhesion energy for the hydrophilic and hydrophobic samples of polysilicon.

Reference/γ_s (unit: mJ m^{-2})	Hydrophilic	Hydrophobic
Mastrangelo and Hsu (1993b)	270 ± 100	100 ± 60
Legtenberg et al. (1994)	260 ± 100 (rinsed by water)	50 ± 50 (rinsed by water)
Legtenberg et al. (1994)	240 ± 100 (rinsed by IPA)	100 ± 50 (rinsed by IPA)
de Boer and Michalske (1999)	16.5 ± 8.2	3.4 ± 0.5
Jones et al. (2003a)	20.6 ± 1.22 (before cyclic loading)	Not available
Jones et al. (2003a)	27.9 ± 0.29 (after cyclic loading)	Not available
Leseman et al. (2007)	15.4 ± 0.6 (rinsed by water)	Not available
Leseman et al. (2007)	13.7 ± 0.7 (rinsed by IPA)	Not available
Rogers et al. (2002)	0.25	Not available

is somewhat incompatible with the contact mechanics of both flexural structures such as beam/plate (Gladwell, 1976; Kerr, 1976, 1979; Zhang, 2008a; Zhang and Murphy, 2004) and "rigid" structures such as sphere (Johnson, 1985, Zhang, 2008b), in which the elastic energy stored inside the contact zone plays a vital role.

Besides the large difference of the adhesion energy measurement, the disputations on the loading history also arise. It is noticed that Eq. (5) actually indicates that the measurement of γ_s is independent of the external load. However, it is seen in Table 1 from the experiments by Jones et al. (2003a) that the loading history has impact on the γ_s measurement. The rinsing liquids are also related to the loading history. The influence of rinsing liquids on the capillary force is indicated by Eq. (1). However, according to the stiction formation theory of a two-step process (Legtenberg et al., 1994), the capillary forces are only responsible for the first step: bringing the MEMS structures into contact with substrate. If the rinsing liquids are completely driven out during the drying process, as indicated by Eq. (5) they should have no influence on the measurement of the adhesion energy (γ_s), which is a solid–solid interfacial energy (Legtenberg et al., 1994; Delrio et al., 2005). As indicated in Table 1, Mastrangelo and Hsu (1993b), de Boer and Michalske (1999), and Rogers et al. (2002) did not consider the influence of the rinsing liquids at all. Legtenberg et al. (1994) designed the experiments using two different rinsing liquids of water and isoproylalchohol (IPA), their conclusion is that the rinsing liquids have no impact on the adhesion energy measurement (though there are some measurement differences between these two rinsing liquids as seen in Table 1). By contrast, Leseman et al. (2007) conducted the experiments using the same two rinsing liquids of water and IPA and concluded that these two liquids have significant impact on the γ_s measurements. Raccurt et al. (2004) designed an experiment to systematically study the influence of rinsing liquids on the adhesion energy measurement of monocrystalline silicon. The three rinsing liquids used by Raccurt et al. (2004) are: de-ioned water (DIW), isoproylalchohol (IPA) and pentane. Table 2 lists the properties of these three rinsing liquids. From

Table 2, the experimental results indicate that the rinsing liquid with larger γ_l results in larger γ_s measurements. Leseman et al. (2007) reached the same conclusion that DIW results in larger strain energy release rate than that of IPA (in the fracture mechanics analysis, the strain energy release rate is equal to γ_s). de Boer et al. (2000) also found that larger voltage (i.e., larger electrostatic external load) induces larger adhesion measurement. Because the previous theory such as Eq. (5) indicates that the surface tension of rinsing liquid (γ_l) has nothing to do with γ_s, Raccurt et al. (2004) argued that the previous theories "should be completed to describe the (rinsing liquid-dependent) experimental results". Raccurt's approach is to incorporate the energy stored in the contact line between liquid and substrate into the system total energy. This liquid–solid interaction energy is omitted in the previous theories (de Boer and Michalske, 1999; Legtenberg et al., 1994; Mastrangelo and Hsu, 1993b; Yang, 2004). In other words, Raccurt's approach assumes that the rinsing liquid is not completely driven out during the drying process, which is the case in some adhered structures (Liu, 2010; Tian and Bhushan, 1996). However, Raccurt's approach may have the difficulty of explaining the experimental observations of "dry" contact by Jones et al. (2003a) that the measured adhesion energy increases after the cyclic loadings exerted by a nanoindenter. Furthermore, Legtenberg et al. (1994) concluded from their experimental analysis that van der Waals (vdW) force and hydrogen bridging are the only two (dominant) mechanisms responsible for the adhesion energy of γ_s; their analysis also excluded the capillary and electrostatic forces as the possible mechanisms. Similarly, Delrio et al. (2005) concluded that when the surface roughness is small, the (normal) vdW force is the (only) mechanism responsible for γ_s; when the surface roughness is large (>50 nm), the retarded vdW force (also known as Casimir force) is the only mechanism responsible for γ_s. Now the third question is raised: (3) *Does the rinsing liquid, or more generally, loading history, have impact on γ_s?*

The contact mechanics model presented in this study aims mainly to answer the three questions raised above. By answering these questions, we hope to resolve some disputations in the MEMS stiction research. The clamped–clamped beam is a common MEMS structures (Legtenberg et al., 1994; Mastrangelo and Hsu, 1993a,b Yang, 2004). By symmetry the contact/stiction of a clamped–clamped beam can be equivalently viewed as the contact/stiction of two cantilevers (Yang, 2004). A contact mechanics model for a clamped–clamped beam under a concentrated load and a uniformly distributed load is presented. It needs to emphasize that stiction here is defined as an attachment state under zero external load. Therefore, some of previous studies (de Boer and Michalske, 1999; Legtenberg et al., 1994; Leseman et al., 2007; Mastrangelo and Hsu, 1993b; Raccurt et al., 2004) do not incorporate the external load. The advantages of incorporating the external load into the model are obvious. For example, Yang (2004) obtained the same stiction results as those obtained by de Boer and Michalske (1999) and Mastrangelo and Hsu (1993b) by reducing the external load to zero; Jones et al. (2003a,b) systematically studied the variation of the load history-dependent adhesion energy by changing the concentrated load exerted by an indenter. Without external load, the analysis in essence can only offer the information on whether the structure is stuck or not; with external load, the structure deformation can be systematically monitored, which is very helpful to those studies on the de-adherence of MEMS structures (Savkar et al., 2007; Zhang and Zhao, 2004, 2005).

2. Model development

Fig. 1 shows a clamped–clamped (C–C) beam under a concentrated load *P* and a uniformly distributed load *q*. The coordinate

Table 2
Properties of DIW, IPA and pentane (Raccurt et al., 2004).

Property/liquid	DIW	IPA	Pentane
Surface tension of γ_l (unit: mJ m^{-2})	73.05	21.7	13.72
Contact angle ($\theta_1 = \theta_2$)	70°	0°	0°
$\gamma_l \cos \theta_1$ (unit: mJ m^{-2})	25.18	21.7	13.72
Measured adhesion energy of γ_s (unit: mJ m^{-2})	163.1	73.97	43.14

system is also shown in the figure. If the beam has no contact with the substrate, the governing equation is as follows:

$$E_1 I \frac{d^4 W}{dx^4} = P\delta(x) + q \tag{6}$$

E_1 is the beam Young's modulus, I is the area moment of inertia defined as $I = BT^3/6$ ($2B$: the beam width and T: the beam thickness). $W = W(x)$ is the beam deflection. $\delta(x)$ is the Dirac delta function. $2L$ is the beam length, L_1/L_2 is the distance from the left/right clamped end to the concentrated load and $2L = L_1 + L_2$. If the concentrated P is located at the center, i.e., $L_1 = L_2 = L$, the following boundary conditions hold for a C–C beam

$$W(-L) = 0, \quad \frac{dW}{dx}(-L) = 0, \quad W(L) = 0, \quad \frac{dW}{dx}(L) = 0 \tag{7}$$

By applying the above boundary conditions, W is solved as follows (Roark, 1954):

$$W = \begin{cases} \frac{P}{48 E_1 I}[6L(x+L)^2 - 4(x+L)^3] + \frac{q(x+L)^2}{24 E_1 I}[(x+L)^2 - 4L(x+L) + 4L^2], & -L \leqslant x \leqslant 0 \\ \frac{P}{48 E_1 I}[6L(-x+L)^2 - 4(-x+L)^3] + \frac{q(x+L)^2}{24 E_1 I}[(x+L)^2 - 4L(x+L) + 4L^2], & 0 \leqslant x \leqslant L \end{cases} \tag{8}$$

When the beam is in contact with the substrate, the governing equation is now changed as the following (Weitsman, 1970; Zhang and Murphy, 2004)

$$\begin{cases} E_1 I \frac{d^4 W_1}{dx^4} = q, & -L_1 < x < x_1 \\ E_1 I \frac{d^4 W_2}{dx^4} + k(W_2 - H) = P\delta(x) + q, & x_1 \leqslant x \leqslant x_2 \\ E_1 I \frac{d^4 W_3}{dx^4} = q, & x_2 < x < L_2 \end{cases} \tag{9}$$

As shown in Fig. 1, W now is divided into three parts: W_2 is the beam displacement in the contact zone; W_1 and W_3 are the displacements in the suspension zones. x_1 and x_2 are the contact separation points, which are the unknowns to be determined. x_1 and x_2 are also the crack tip locations from the viewpoint of fracture mechanics (de Boer and Michalske, 1999; Jones et al., 2003a,b; Knapp and de Boer, 2002). $x_2 - x_1 = 2A$ is the beam contact length. k is the modulus of elastic foundation. H is the gap distance between the undeformed beam and substrate. $-k(W_2 - H)$ is thus the contact pressure exerted by the substrate on the beam. For a prismatic beam indenting an elastic substrate, k is given as follows (Biot, 1937)

$$k = 0.71 E_2 \left(\frac{E_2 B^4}{E_1 I} \right)^{1/3} \tag{10}$$

E_2 is the Young's modulus of substrate. An implicit assumption used in Eq. (9) is that the concentrated load P is within the contact zone. The concentrated load can be outside the contact zone (Jones et al., 2003a; Zhang and Zhao, 2011). In this study, only the symmetric loading of the concentrated load located at the beam center is studied and the beam center displacement is the maximum displacement. The concentrated load is thus guaranteed to be within the contact zone. Eq. (9) also assumes small linear elastic deformation for both the beam and substrate.

The following nondimensionalization scheme is introduced (Weitsman, 1970; Zhang, 2008)

$$\xi = \beta x, \quad w_i = \beta W_i \ (i = 1,2,3), \quad \xi_1 = \beta x_1, \quad \xi_2 = \beta x_2,$$
$$h = \beta H, \quad a = \beta A, \quad l_1 = \beta L_1, \quad l_2 = \beta L_2, \quad l = \beta L,$$
$$F = \frac{P}{4\beta^2 E_1 I}, \quad Q = \frac{q}{\beta^3 E_1 I} \tag{11}$$

β is defined as (Weitsman, 1970; Zhang and Murphy, 2004)

$$\beta = \sqrt[4]{\frac{k}{4 E_1 I}} \tag{12}$$

Substitute k of Eq. (10) into Eq. (12), β is found as $\beta \approx 1.18 \left(\frac{E_2}{E_1} \right)^{1/3} \frac{1}{T}$. For two solids with similar Young's moduli (i.e., $E_1 \approx E_2$), $\beta \approx 1/T$ and β has the unit of m^{-1}. In other words, the nondimensionalization scheme of Eq. (11) on the beam dimensions is to give the ratios of the beam dimensions to its thickness. For example, $l = \beta L \propto L/T$ in essence indicates the slenderness of beam. As a rule of thumb, for a chunky beam of $\frac{T}{2L} > \frac{1}{7}$, the contribution of shear force to the beam deformation needs to be considered and the Timoshenko beam model applies. Both Eqs. (6) and (9) use the Euler–Bernoulli beam model.

Eq. (7) is now nondimensionalized as the following

$$w(-l) = 0, \quad \frac{dw}{d\xi}(-l) = 0, \quad w(l) = 0, \quad \frac{dw}{d\xi}(l) = 0 \tag{13}$$

Eq. (8) is nondimensionalized as

$$w = \begin{cases} \frac{F}{12}[6l(\xi+l)^2 - 4(\xi+l)^3] + \frac{Q(\xi+l)^2}{24}[(\xi+l)^2 - 4l(\xi+l) + 4l^2], & -l \leqslant \xi \leqslant 0 \\ \frac{F}{12}[6l(-\xi+l)^2 - 4(-\xi+l)^3] + \frac{Q(\xi+l)^2}{24}[(\xi+l)^2 - 4l(\xi+l) + 4l^2], & 0 \leqslant \xi \leqslant l \end{cases} \tag{14}$$

Eq. (9) is nondimensionalized as the following

$$\begin{cases} w_{1\xi\xi\xi\xi} = Q, & -l_1 < \xi < \xi_1 \\ \frac{1}{4} w_{2\xi\xi\xi\xi} + w_2 - h = F\delta(\xi) + \frac{Q}{4}, & \xi_1 \leqslant \xi \leqslant \xi_2 \\ w_{3\xi\xi\xi\xi} = Q, & \xi_2 < \xi < l_2 \end{cases} \tag{15}$$

Here $()_{,\xi} = \frac{d}{d\xi}$. The solution forms to Eq. (15) are given as follows (Zhang and Murphy, 2004)

$$w = \begin{cases} w_1 = A_1 \xi^3 + B_1 \xi^2 + C_1 \xi + D_1 + \frac{Q}{24} \xi^4 \\ w_2 = A_2 \cosh \xi \sin \xi + B_2 \cosh \xi \cos \xi + C_2 \sinh \xi \sin \xi + D_2 \\ \quad \sinh \xi \cos \xi - \frac{F}{2} \sinh |\xi| \cos \xi + \frac{F}{2} \cosh \xi \sin |\xi| + \frac{1}{4} Q + h \\ w_3 = A_3 \xi^3 + B_3 \xi^2 + C_3 \xi + D_3 + \frac{Q}{24} \xi^4 \end{cases} \tag{16}$$

A_i, B_i, C_i and D_i (i = 1, 2 and 3) are 12 unknown constants to be determined. These 12 unknowns together with ξ_1 and ξ_2 are the 14 unknowns in total to be solved.

At the contact separation points of x_1 and x_2, the following eight so-called transversality conditions can be derived via a variational approach (Kerr, 1976), which indicate the continuity of the displacement, slope, moment and shear force (Zhang, 2010).

$$w_1(\xi_1) = w_2(\xi_1), \quad \frac{dw_1}{d\xi}(\xi_1) = \frac{dw_2}{d\xi}(\xi_1), \quad \frac{d^2 w_1}{d\xi^2}(\xi_1) = \frac{d^2 w_2}{d\xi^2}(\xi_1), \quad \frac{d^3 w_1}{d\xi^3}(\xi_1) = \frac{dw_2}{d\xi^2}(\xi_1),$$
$$w_2(\xi_2) = w_3(\xi_2), \quad \frac{dw_2}{d\xi}(\xi_2) = \frac{dw_3}{d\xi}(\xi_2), \quad \frac{d^2 w_2}{d\xi^2}(\xi_2) = \frac{d^2 w_3}{d\xi^2}(\xi_2), \quad \frac{d^3 w_2}{d\xi^3}(\xi_2) = \frac{d^3 w_3}{d\xi^3}(\xi_2) \tag{17}$$

The same transversality conditions as Eq. (17) are also obtained by Ghatak et al. (2005). The following two equations are obtained by minimizing the system total energy (Appendix B)

$$w_2(\xi_1) = h - \sqrt{\alpha}/2, \quad w_2(\xi_2) = h - \sqrt{\alpha}/2 \tag{18}$$

α is a dimensionless parameter defined as

$$\alpha = \frac{4B\gamma_s}{E_1 I \beta^2} \tag{19}$$

When there is no adhesion ($\alpha = 0$), Eq. (18) recovers those of the non-adhesive contact case (Zhang and Murphy, 2004).

The arc-shaped deformation assumes the hinged conditions at the contact separation point, which are $w_1(\xi_1) = h$ and $\frac{d^2 w_1}{d\xi^2}(\xi_1) = 0$. As mentioned before, the zero bending moment condition of $\frac{d^2 w_1}{d\xi^2}(\xi_1) = 0$ at the contact separation points has been used by Timoshenko (1956) and Weitsman (1970). Yang (2004) argued that the zero bending moment assumption at the contact

separation point cannot be valid for adhesive contact. Zhang and Murphy's (2004) computation shows that only when the beam is very slender, can such assumption be a good approximation. The S-shaped deformation assumes the clamped conditions at the contact separation point, which are $w_1(\xi_1) = h$ and $\frac{dw_1}{d\xi}(\xi_1) = 0$ of zero rotation angle. In contrast, Eq. (17) does not prescribe the zero bending moment or zero rotation angle at the contact separation point. Physically the contact deformation between the beam and substrate in general does not allow the zero moment or zero rotation angle at the contact separation point. It is also noticed that in Eq. (18) the displacement at the contact separation points is $h - \sqrt{\alpha}/2$ rather than h of both arc-shape and S-shape. Because the contact pressure is $-k(W_2 - H)$, there are two zones around x_1 and x_2 having tensile pressure (positive value of $-k(W_2 - H)$) and an inner zone with compressive contact pressure (negative value of $-k(W_2 - H)$), which resembles the adhesive contact scenario of spheres described by the Johnson–Kendall–Roberts (JKR) model (Johnson, 1985). Eq. (18) is derived by assuming that the beam is already in contact with substrate, which is governed by Eq. (9). If the beam has no contact with the substrate, the governing equation is Eq. (6).

Eqs. (13), (17) and (18) offer 14 equations in total to solve the 14 unknowns. Because of the unknown property of ξ_1 and ξ_2, solving these 14 unknowns is a highly nonlinear problem and the Newton–Rhapson method (Press et al., 1992) is required. To apply the Newton–Rhapson method, one needs to guess a set of values for A_i, B_i, C_i, D_i (i = 1, 2 and 3), ξ_1 and ξ_2 for a given external load. Fortunately, the computation is not (very) sensitive to the initial guessed values.

3. Results and discussion

In all the figures presented in this paper, h is fixed as 1. Fig. 2 shows the deformations of a chunky beam under a concentrated load, a uniformly distributed load and no load, respectively. In Fig. 2, $2l = 10$ and $\alpha = 0.02$. α is defined in Eq. (19) as $\alpha = 4B\gamma_s/(E_1 I \beta^2) \propto 24 \frac{\gamma_s}{E_1} \frac{1}{T}$. γ_s/E_1 is quite small, which is around 10^{-9}–10^{-12} m (Giri et al., 2001; Miller and Shenoy, 2000; Sun et al., 2004) for various materials. Usually the MEMS structure thickness is around 10^{-6} m or larger. Therefore, $\alpha = 0.02$ physically indicates a strong adhesion for a MEMS structure. The purpose of selecting this large α value is to emphasize the effect of adhesion.
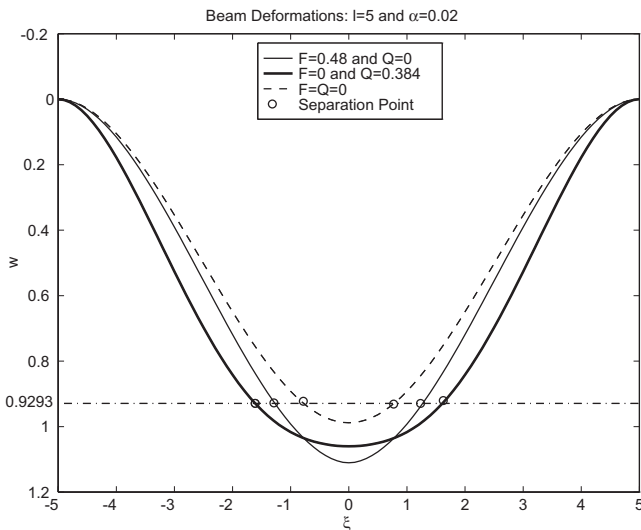

Fig. 2. The "chunky" beam deformation shapes with the concentrated load, distributed load and zero load, respectively. $2l = 10$ and $\alpha = 0.02$.

The concentrated load is taken as $F = 10 \times \frac{48h}{(2l)^3} = 0.48$ and the distributed load is taken $Q = 10 \times \frac{384h}{(2l)^4} = 0.384$. According to Roark (1954), the center displacement of a C–C beam with a span of $2L$ is $W_c = \frac{P(2L)^3}{192E_1 I}$ under a concentrated load P located at the center and $W_c = \frac{q(2L)^4}{384E_1 I}$ under a uniformly distributed load q. These two center displacements is nondimensionalized as $w_c = \frac{F(2l)^3}{48}$ and $w_c = \frac{Q(2l)^4}{384}$, respectively. Because h is fixed as 1, the center displacement of a C–C free-standing beam under a concentrated load of $F = 0.48$ or a distributed load of $Q = 0.384$, respectively, reaches $10h$. Therefore, with this selection of F and Q, the beam is guaranteed to have contact with the substrate. With the concentrated load of $F = 0.48$ (and $Q = 0$), the half contact length is $a = -\xi_1 = \xi_2 = 1.271$ and the beam center displacement is $w_c = 1.111$. As indicated by Eq. (18), the beam separates from the substrate when $w = h - \sqrt{\alpha}/2 = 0.9293$, which occurs correspondingly at $-\xi_1 = \xi_2 = 1.271$ for the concentrated load of $F = 0.48$. $-\xi_1 = \xi_2 = 1.61$ for the distributed load of $Q = 0.384$. Under different loadings, the deformations of beam in contact are different: the distributed load has larger contact length ($2a = 2 \times 1.61$) and shallower indentation depth ($w_c = 1.06$) in comparison with $2a = 2 \times 1.61$ and $w_c = 1.111$ of the concentrated load of $F = 0.48$. The curve of $F = Q = 0$ physically corresponds to the stiction state. This curve is obtained by reducing F or Q to zero from a contact state. Whether the beam is initially under a concentrated load or a distributed load has no impact on this stiction curve. The magnitude of concentrated load and distributed load has no impact, either. Because the type and magnitude of external load have no influence on the final stiction curve, it is in contradiction with the aforementioned experimental observations by Leseman et al. (2007) and Raccurt et al. (2004). The different rinsing liquids used in Leseman's and Raccurt's experiments in essence offer different (nonlinear) distributed load of Q. This contradiction will be explained later. With the retraction of load, the half contact length of $F = Q = 0$ reduces to $a = -\xi_1 = \xi_2 = 0.777$ and the center displacement shrinks to $w_c = 0.988$. It is noticed that this center displacement, which is also the maximum displacement is less than h (h = 1). The contact pressure is defined as $\sigma = -k(W - H)$. Fig. 3 plots the profiles of contact pressure. $\sigma\beta/k = -(w - h)$ is the dimensionless pressure; the positive values indicate the tensile pressure and negative ones are compressive. In Fig. 3, for the case of zero external load, the whole contact pressure is tensile. From the force equilibrium point of view, when there is no external load, the restoring force of the deformed beam is trying to pull the beam back to its original straight/undeformed equilibrium configuration. This tensile contact pressure due to adhesion is responsible for balancing this restoring force and keeping the beam in a deformed shape. For $F = 0.48$ and $Q = 0.384$, compressive contact pressure exists in the inner contact zone and tensile contact pressure is in the outer contact zone. The same scenario occurs in the JKR model for a sphere contact. In the JKR contact model, the contact area is divided into two parts: the outer annulus zone with tensile pressure induced by adhesion and inner circular zone with compressive pressure (Johnson, 1985; Zhang, 2008b). The outer annulus zone dominates when the external load is tensile or the compressive external load is small; the inner circular zone dominates when
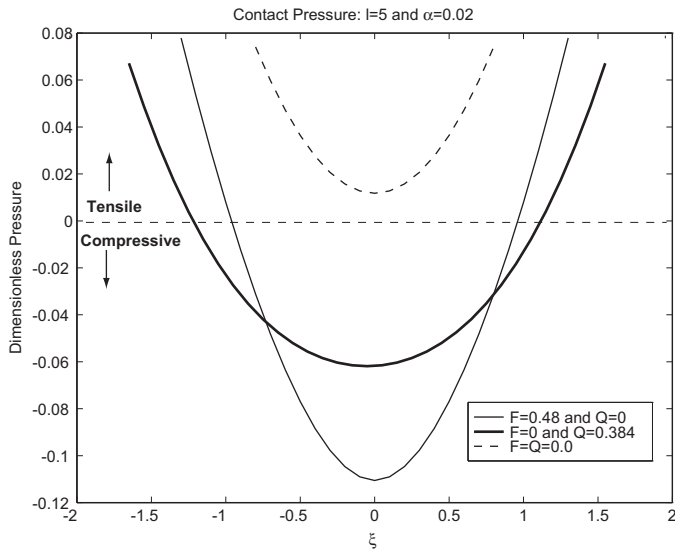
Fig. 3. The dimensionless contact pressure ($\sigma\beta/k$) profiles of the beam with the concentrated load, distributed load and zero load, respectively. $2l = 10$ and $\alpha = 0.02$.

the external compressive load is large (Zhang, 2008b). As F or Q is reduced, the compressive contact zone shrinks (Zhang, 2008b) and finally, as shown in Fig. 3, the compressive zone is gone and only the tensile zone is left. Because the elastic energy due to the contact deformation is not accounted, the previous models such as the energy approach (Legtenberg et al., 1994; Mastrangelo and Hsu, 1993b; Raccurt et al., 2004; Yang, 2004) and the fracture mechanics approach (de Boer and Michalske, 1999; de Boer et al., 1999; Knapp and de Boer, 2002; Jones et al., 2003a; Leseman et al., 2007) are unable to provide such contact pressure analysis.

In Fig. 2, the curve of $F = Q = 0$ is obtained by reducing F or Q to zero, which physically corresponds to the unloading scenario. In the loading process, the beam can only make the initial contact when the beam center displacement exceeds h. Before contact, the beam equilibrium is governed by Eq. (6); after contact, the

beam equilibrium is governed by Eq. (9). The switch of these two governing equations leads to the so-called "jump-in" phenomenon as shown in Fig. 4. In Fig. 4 the beam with $2l = 10$ and $\alpha = 0.02$ is under a distributed load Q only. As Q varies from 0 to 0.0384, no contact occurs. Therefore, the half-contact a remains zero and the center displacement increases linearly from 0 to 1. At $Q = 0.0384$, $w_c = \frac{Q(2l)^4}{384} = 1$ is the critical point that the beam center makes its initial contact with the substrate. Once Q surpasses this critical values, the beam is in contact with the substrate, which results in a discontinuous change (jump-in) of a and w_c. As shown in Fig. 4(a), the half contact a changes abruptly from 0 to 1.19 and w_c jumps from 1 to 1.031 at $Q = 0.0384$. If Q continues to increase, a and w_c will keep increasing continuously as indicated by those loading arrows. In Fig. 4(b) one observation is that the slope becomes significantly smaller after jump-in and this slope changing behavior is also reported by Jones et al. (2003a,b). Physically this smaller slope means larger stiffness and obviously the stiffness increase is due to the initiation of contact between the beam and substrate. If Q is reduced, a and w_c follow the paths as indicated by the unloading arrows. When $Q = 0$, stiction is found with $a = 0.777$ and $w_c = 0.988$. Fig. 5 shows the beam deformation shapes just before and after jump-in at $Q = 0.0384$. Before jump-in, the beam center displacement just reaches h of 1 and the beam contact length is zero; after jump-in, the beam center displacement becomes as $w_c = 1.031$ and the contact length becomes as $2 \times 1.19 = 3.38$. With the presence of adhesion, the beam starts with a finite contact length rather than a point contact, which is also observed by Liu (2010). The arc-shape is a point contact scenario and this contact initiation with finite length also contributes to the difference of deformation shapes.

It is worth pointing out that the jump-in phenomenon discussed here is different from the one analyzed by Mastrangelo and Hsu (1993a) and Legtenberg et al. (1994). Mathematically the jump-in here is caused by the switch of the governing equations and physically adhesion is the mechanism. In Fig. 4 the unloading path is governed by Eq. (9); the loading path is governed by Eq. (6) and then by Eq. (9). For the loading of a free-standing beam, the contact initiates only when w_c exceeds h. However, for the unloading of a contacted beam, the displacement at the separation points is $w(\xi_1) = w(\xi_2) = h - \sqrt{\alpha}/2 = 0.9293$ (for $\alpha = 0.02$ and $h = 1$). So the difference between the critical displacements
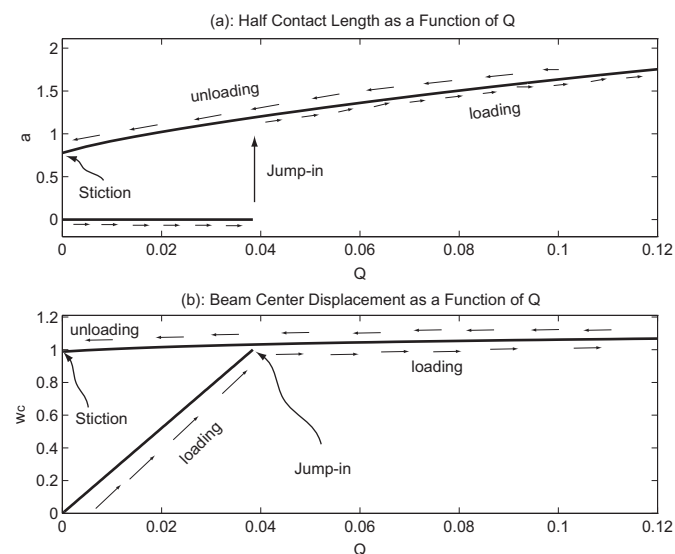

Fig. 4. (a) The half contact length a as a function of the distributed load Q. (b) The beam center displacement w_c as a function of Q. $2l = 10$ and $\alpha = 0.02$. Jump-in occurs at $Q = 0.0384$, at which the beam center just touches the substrate.
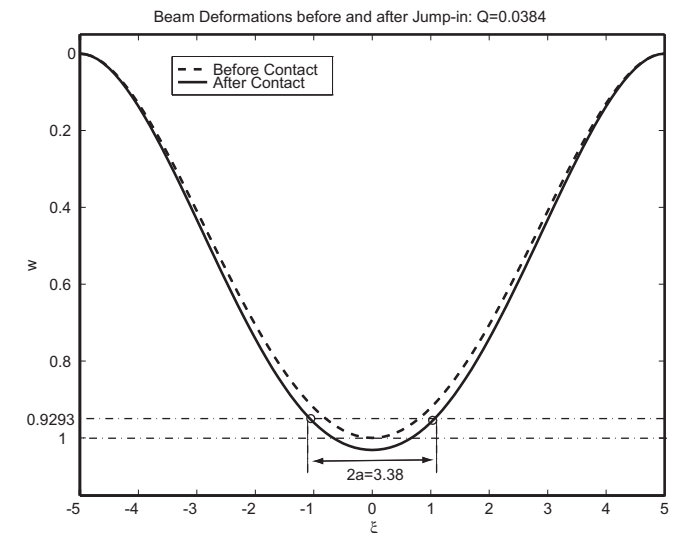

Fig. 5. The beam deformation shapes just before and after jump-in at $Q = 0.0384$. Before jump-in, the beam center displacement just reaches h of 1 and is with zero contact length; after jump-in, the beam center displacement becomes as $w_c = 1.031$ and contact length becomes as $2 \times 1.19 = 3.38$.

for contact initiation and separation is $\sqrt{\alpha}/2$. When $\alpha \neq 0$, the beam experiences the abrupt changes of the deformation shape and contact length as shown in Fig. 5. Only when $\alpha = 0$, the jump-in phenomenon can be eliminated and a point contact can be formed (Zhang and Murphy, 2004). Instead of constant load of Q or F, the external load used by Mastrangelo and Hsu (1993a) and Legtenberg et al. (1994) is capillary force. The structure restoring force varies linearly with its displacement and the capillary force varies nonlinearly as indicated by Eq. (1). When the displacement reaches a critical value at which the restoring force can no longer balance the capillary force, jump-in occurs. Usually when such jump-in occurs, the beam center displacement is around 1/3 of the gap distance (Zhang and Zhao, 2006). The in-depth analysis by Mastrangelo and Hsu (1993a) on the system total energy reveals that their jump-in is the saddle node type of instability, which is the same type for the case of the external load as an electrostatic force (Zhang and Zhao, 2006).

Fig. 6 shows how the α parameter influences the jump-in and jump-off. All jump-ins occur during the loading process at $Q = 0.0384$ when the beam center touches the substrate. a jumps from 0 to 0.8145 ($\alpha = 0.005$), 0.9796 ($\alpha = 0.01$), 1.0957 ($\alpha = 0.015$) and 1.19 ($\alpha = 0.02$), respectively; w_c jumps from 1 to 1.0164 ($\alpha = 0.05$), 1.0229 ($\alpha = 0.01$), 1.0277 ($\alpha = 0.015$) and 1.031 ($\alpha = 0.02$). The jump-in magnitudes of both a and w_c reduce monotonously as α decreases. The jump-off, which is variably called as peel-off or pull-off (Johnson, 1985; Zhang, 2008b), is observed during the unloading process. The abrupt separation behavior of jump-off is also predicted by the JKR model for the adhesive spheres contact (Johnson, 1985; Zhang, 2008b). Except for the case of $\alpha = 0.02$, which leads to stiction, the other three cases all experience sudden separation from contact. For $\alpha = 0.005$, the jump-off occurs at $Q = 2.11 \times 10^{-2}$; for $\alpha = 0.01$, the jump-off occurs at $Q = 9.6 \times 10^{-3}$; for $\alpha = 0.015$, the jump-off occurs at $Q = 1.92 \times 10^{-3}$. The critical Q at jump-off increases monotonously as α decreases. Physically it is not difficult to understand this observation: smaller α means less tensile contact pressure generated by adhesion and the beam needs the help of larger external load to balance the restoring force. When α is large (such as the case of $\alpha = 0.02$ here), the adhesive tensile contact pressure alone can balance the restoring force, which is the stiction case. For $\alpha = 0.02$, Q needs to be further reduced to a negative value to de-adhere the stuck beam.

Fig. 7 compares our beam deformation with the arc-shape and S-shape. The beam is with the length of $2l = 10$ and $\alpha = 0.02$. Because of the symmetry, we plot half of the beam deformation. The suspension length of the arc-shaped beam is $s_{arc} = \sqrt[4]{9h^2/\alpha} = 4.606$ and that of the S-shaped beam is $s_{c-c} = \sqrt[4]{36h^2/\alpha} = \sqrt{2}s_{arc} = 6.514$ (Appendix A). If the beam is assumed to deform as the S-shape, $s_{c-c} > l$ ($l = 5$) and therefore, no stiction can occur. However, our model and arc-shape predict the stiction. The suspension length is predicted by our model as $s = 4.012$, which is even shorter than that of the arc-shape. The beam/substrate contact predicted by our model starts at $\xi = s - l = -0.988$ with the corresponding displacement of $w(-0.988) = 0.9293$; the arc-shaped beam has a point contact with the substrate at $\xi = s_{arc} - l = -0.394$ with $w(-0.394) = h = 1$; the S-shaped beam contacts the substrate at $\xi = s_{c-c} - l = 1.514$ with $w(1.514) = h = 1$. In Fig. 7 the beam deformation shape of our model does not resemble either S-shape or arc-shape. However, if the arc-shape or S-shape must be chosen to approximate the deformation shape of this chunky beam, the arc-shape is a much better approximation. For the adhesion measurement of using Eq. (5), the deformation shape deviation from arc-shape and S-shape can be a significant factor contributing to the large measurement difference.

Fig. 8 examines the deformation shapes of a slender beam deform. The beam is with the length of $2l = 30$ and $\alpha = 0.02$. The concentrated load is taken as $F = 10 \times \frac{48h}{(2l)^3} = 0.018$ and the uniformly distributed load is taken as $Q = 10 \times \frac{384h}{(2l)^4} = 0.00474$. The selection of these concentrated and distributed loads is to let $w_c = 10h$ for a free-standing beam to assure the contact. The curve of $F = Q = 0$ is obtained by reducing F or Q to zero from a contact state; the loading type (concentrated or distributed) and magnitude have no impact on the stiction state. In Fig. 8 the three deformation curves are almost indistinguishable from one another. Compared with the chunky beam, a relative large portion of the slender beam is flattened around its center. Now the half contact length becomes $a = -\xi_1 = \xi_2 = 9.52$ at $F = Q = 0$. The ratio of contact length to the beam length now becomes as $a/l = 63.5\%$ compared with $0.988/5 = 19.8\%$ of the chunky beam. Fig. 9 examines the contact pressure distribution of this slender beam. As seen in Fig. 8 the three deformation curves are almost indistinguishable, we only
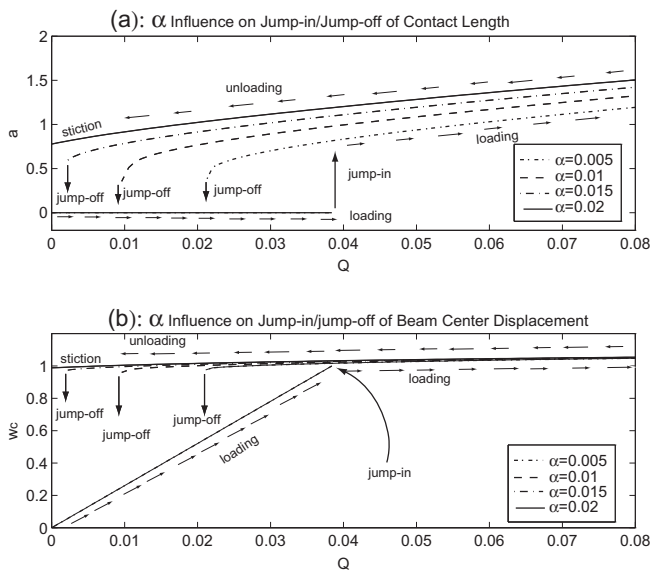

Fig. 6. (a) The half contact length a as a function of the distributed load Q. (b) The beam center displacement w_c as a function of Q. $2l = 10$ and now α varies as 5×10^{-3}, 1×10^{-2}, 1.5×10^{-2} and 2×10^{-2}. For the beam with different αs, jump-in always occur at $Q = 0.0384$. During unloading, except the case of $\alpha = 2 \times 10^{-2}$, all other three cases jump-off at different Qs. The trend is clear: beam with a larger α jumps-off at a smaller Q.
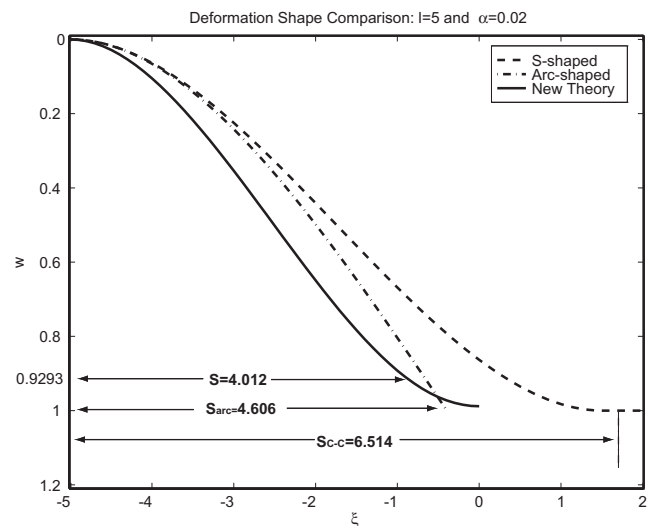

Fig. 7. Comparison of our beam deformation shape with arc-shape and S-shape. $2l = 10$ and $\alpha = 0.02$.
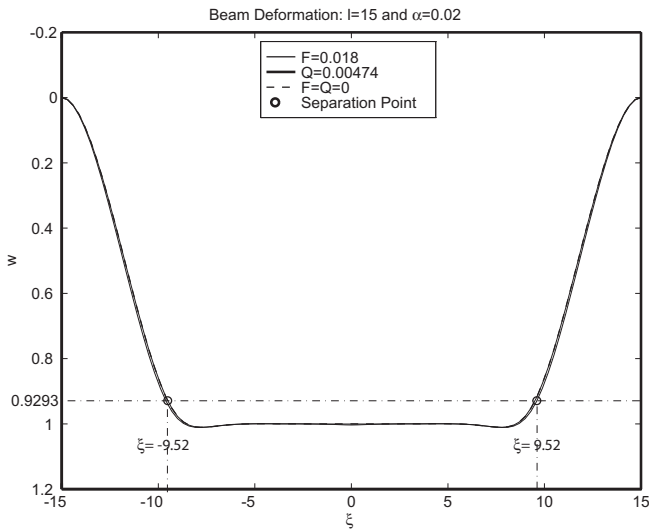
Fig. 8. The slender beam deformation shapes with the concentrated load, distributed load and zero load, respectively. $2l = 30$ and $\alpha = 0.02$.
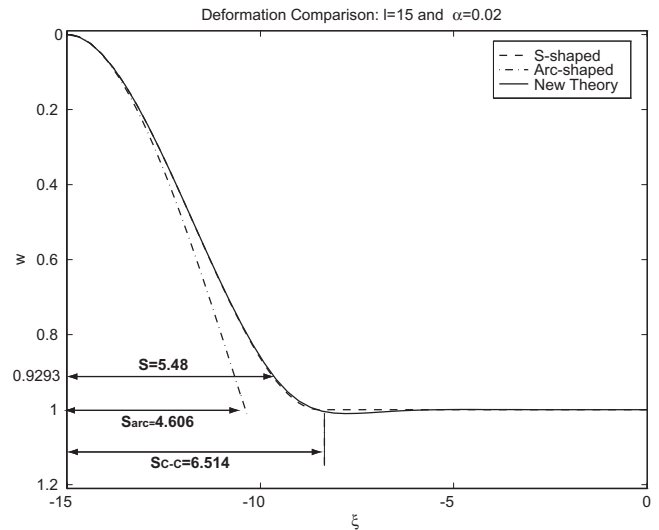

Fig. 10. Comparison of our beam deformation shape with arc-shape and S-shape. $2l = 30$ and $\alpha = 0.02$.
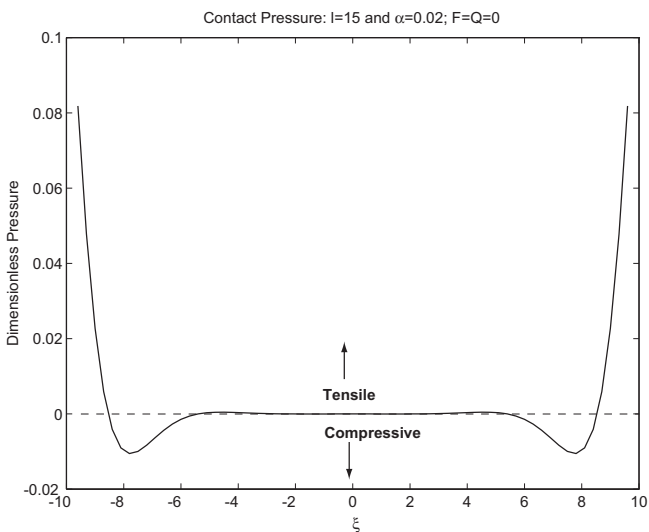

Fig. 9. The contact pressure profiles of the beam with zero external load. $2l = 30$ and $\alpha = 0.02$.

Fig. 11. The suspension length as a function of l.

plot the dimensionless contact pressure $\sigma\beta/k = -(w - h)$ of the stiction state of $F = Q = 0$ in Fig. 9. Around the contact edge, the contact pressure experiences a rapid tensile-compressive pressure transition and then approaches to zero. In comparison, at the stiction state of $F = Q = 0$, only the tensile contact pressure exists in the contact zone of a chunky beam. The tensile contact pressure of a chunky beam only needs to balance the beam restoring force at the stiction state; however, the tensile contact pressure of a slender beam has to balance the beam restoring force plus the compressive contact pressure.

Fig. 10 compares the deformation shape of the slender beam with the arc-shape and S-shape. The S-shaped deformation approximates our beam deformation fairly well: most parts are overlapped except some parts around the contact edge. Although our beam deformation shape is very close to the S-shape, their suspension lengths and rotation angles at the contact separation points are still quite different. The suspension length of the slender beam now is $s = l - a = 5.48$. Because the suspension lengths predicted by the arc-shaped and S-shaped deformations do not change
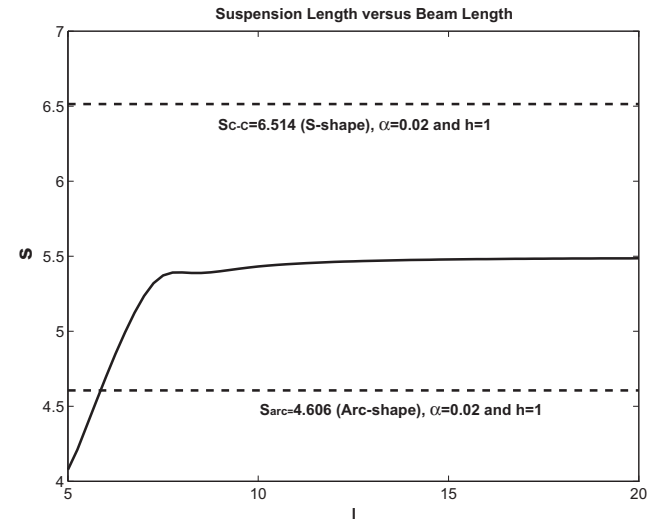
with the variation of beam length, they still remain the same as $s_{arc} = 4.606$ and $s_{c-c} = 6.514$. The S-shaped beam separates from substrate at $\xi = s_{c-c} - l = -8.486$ and the rotation angle is zero at the separation point because of its clamped condition; our beam separates from the substrate at $\xi = \xi_1 = -9.52$ and the rotation angle is $\arctan(0.1196) \approx 6.8^o$. This small rotation angle at the contact separation point(s) is in agreement with de Boer and Michalske's (1999) observations. Fig. 11 plots the suspension length (s) as a function of l. s starts as 4.012 at $l = 5$, increases monotonously and then converges to $s = 5.48$, which is much smaller than s_{c-c}. Although the S-shape deformation is almost identical to our beam deformation of slender beam, the suspension length and rotation angle are different. The elastic energy due to contact deformation and the bending energy inside contact zone result in the difference between our total system energy (as calculated in Appendix B) and that of assuming the S-shape or arc-shape deformation, which is responsible for the deviation of our deformation shape from the arc-shape or the S-shape.

Now the first two questions raised in Section 1 can be answered. At the stiction state, the beam deforms neither as the arc-shape nor

as the S-shape; the transversality conditions at the separation point(s) are neither the clamped ones nor the hinged ones but the ones described in Eq. (17). The arc-shape better approximates the stiction shape of a chunky beam and the S-shape better approximates that of a slender beam. However, the difference as shown in Figs. 7 and 10 is still significant. Eqs. (3) and (5) assume the arc-shaped or S-shaped deformation, which can lead to deviation or even erroneous predictions on the critical suspension length and adhesion energy. The previous studies on MEMS stiction (de Boer and Michalske, 1999; de Boer et al., 1999; Jones et al., 2003a; Rogers et al., 2002) do not have a criterion to tell when the arc-shaped or S-shaped deformation is formed. The two dimensionless parameters of α and l are the reasons for the deformation shape change. Evans and Lauga (2009) conducted a computation to show the transition between the arc-shape and S-shape (they called S-shape as clamped shape) of two flexible sheets. Rather than using the concept of adhesion energy, Evans and Lauga (2009) used the vdW interaction forces between two sheets and defined a dimensionless Ω to show the transition. Evans and Lauga's (2009) Ω indicates the (order of) the ratio of the vdW force to the elastic one and $\Omega \propto \gamma_s L^3$, which essentially plays the same role of α and l. Of course, there are other factors impacting the deformation shape, for example, the residual stress inside the flexural structure (Wong et al., 2007). The residual stress is not considered in this study for the comparison reason because the arc-shaped and S-shaped deformations are residual stress-free (Appendix A).

Fig. 12 is introduced to answer the third question of the γ_s dependence on the loading history. The Euler–Bernoulli beam theory of Eqs. (6) and (9) only describes the deflection of the beam neutral axis. It needs to keep in mind that the adhesion energy measured by using Eq. (5) is a nominal one, which is much smaller than a real one (Knapp and de Boer, 2002; Zhao et al., 2003). The actual contact area of the two contacting bodies with rough surfaces as shown in Fig. 12 is very small compared with the nominal one. Therefore, the adhesion energy measured by the microbeam stiction test as listed in Table 1 is about three orders of magnitude smaller than the lowest adhesion energy observed in nature (Knapp and de Boer, 2002). Several models (Fuller and Tabor, 1975; Greenwood and Tripp, 1967; Greenwood and Williamson, 1966; Hariri et al., 2006; Tas et al., 2003; van Spengen et al., 2002; Yu and Suo, 1998) are developed to attack this surface roughness issue. However, extreme caution should be taken when applying those models to the contact problem of flexural structures. The above contact models of rough surfaces are developed for "rigid" contacting bodies such as spheres and very chunky plate-like structures. Those "rigid" contacting bodies do not deflect during contact and only small deformation occurs in and around

A Closer Look at the Beam Contact Edge

Fig. 12. A closer look at the contact of two rough surfaces.

the contact zone. For example, the Hertz and JKR models of spheres contact assume that the dimension of contact are extremely small in comparison with that of spheres and the radius of curvature is thus assumed to be constant for different external loadings (Johnson, 1985, Zhang, 2008b). The constant radius of curvature prescribes the sphere contact deformation and leads to the conclusion of a flat contact zone (Zhang, 2008b). The deflection change of a flexural structure is significant under different external load, so is its radius of curvature. As seen in Figs. 2 and 8, the contact zones of the flexural beam are not flat. Knapp and de Boer (2002) observed that the adhesion measurement is highly sensitive to external load and the shape of the deflection curve. So far we are unable to establish or find the model for the contact problem of flexural structure with rough surfaces. However, the mechanisms discussed in those models on the rough surface contact of "rigid" structures can offer some insights on how the loading history dependent adhesion energy measurement occurs (de Boer et al., 2000; Leseman et al., 2007; Raccurt et al., 2004).

In the contact of two rough surfaces, the system total energy increases due to the deformations of asperities and decreases due to the reduction of surface area (Fuller and Tabor, 1975; Yu and Suo, 1998). Fuller and Tabor (1975) defined the following dimensionless parameter known as adhesion parameter, θ:

$$\theta = \frac{E' \sigma_d^{3/2} \beta_r^{1/2}}{\beta_r \gamma_s'} \tag{20}$$

$1/E' = (1 - v_1^2)/E_1 + (1 - v_2^2)/E_2$. v_1, v_2 and E_1, E_2 are the Poisson's ratios and Young's moduli of two contacting bodies, respectively. σ_d is the standard deviation of the height distribution of a rough surface. The summits of all asperities are assumed to have a radius of β_r. γ_s' is the real adhesion energy, which is a fixed value for the given materials of two contacting bodies. Eq. (20) is derived by the JKR model of the "rigid" spheres. θ in essence indicates the statistical average of the competition between the elastic restoring force (due to the surface asperities deformations only) and adhesion force. The numerator is a measure of the elastic force needed to push a sphere of radius β_r to a depth σ_d into an elastic solid of modulus E'; the denominator is a measure of the adhesive force experienced by a sphere of radius β_r (Fuller and Tabor, 1975). The adhesion force tries to hold the surfaces together and the compressive force due to the asperities deformations tries to push the surfaces away. Small θ indicates that adhesion dominates and large θ indicates that compressive force due to elastic deformation of asperities dominates. Yu and Suo (1998) conducted a more detailed study for an idealized peak-to-peak contact of two rough surfaces and developed the gap-closing criteria. Besides σ_d, Yu and Suo (1998) showed that the wavelength of asperities and thickness of two contacting chunky wafers also play important roles. The elastic theory on the asperity contact itself cannot offer the explanation on the third question. In both the models (Fuller and Tabor, 1975; Yu and Suo, 1998), the external load does not appear as a parameter, which implies that the final stiction state is independent of the external load. Our model is also an elastic model and the discussions on Figs. 2 and 8 show that the stiction state is independent of external load. In that sense, our model is consistent with the above two models (Fuller and Tabor, 1975; Yu and Suo, 1998). However, the surface asperity can also experience the irreversible plastic deformation. Greenwood and Williamson (1966) defined the following dimensionless parameter called plasticity index

$$\psi = \frac{E'}{H'} \sqrt{\frac{\sigma_d}{\beta_r}} \tag{21}$$

H' is the material hardness. If $\psi < 0.6$, plastic contact can only be caused when the surfaces are forced together by very large pressure; If $\psi > 1$, plastic contact occurs even at trivial pressure
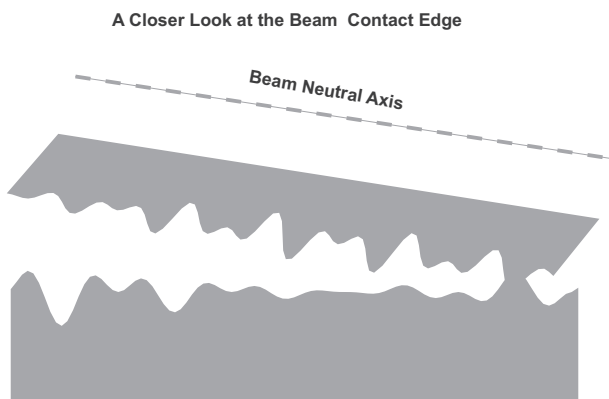
(Greenwood and Williamson, 1966). Eq. (21) is developed by the Hertz model of the "rigid" spheres. Again, the external load does appear as an influencing factor in Eq. (21). However, things are quite different in our model: as shown in Fig. 12 the beam deflection as indicated by its neutral axis is determined by the external load type and magnitude, which is vital to determining the contact pressure and thus plastic deformation. The permanent plastic deformation reduces σ_d, which enhances the adhesion influence as indicated by Eq. (20). This is the reason for the experimental observations by Jones et al. (2003a) that the measured adhesion energy increases after cyclic loadings as listed in Table 1. Jones et al. (2003b) also found in their test of an 100 μm long beam that during the first load cycle, there is a total energy change of 149.8 pJ and they estimated the dissipated energy is responsible for 111 pJ of this 149.8 pJ of total energy change; after 6–15 cycles, they found that there is a repeatable total energy change of 43.23 ± 2.29 pJ, i.e., no dissipated energy. It is not hard to use Eq. (21) to give a qualitative explanation on Jones et al.'s (2003b) observation. Plastic deformation dissipates energy and the area between the loading and unloading curves indicates the dissipated energy. Most plastic deformation occurs in the first load cycle, which significantly reduces σ_d. As a result, smaller σ_d makes the plastic deformation more difficult to occur as indicated by Eq. (21). After several load cycles, σ_d is small enough, there is no more plastic deformation and thus no energy dissipated. In general, larger external load (either electrostatic load (de Boer et al., 2000) or mechanical load (Jones et al., 2003a,b) or capillary load (Leseman et al., 2007; Raccurt et al., 2004)) is expected to induce more plastic deformation and thus reduce σ_d. Also, larger external load induces larger deformations of asperities (both elastic and plastic), which shrinks the gap distances between two rough surfaces. For "wet" contact, the capillary forces of the trapped liquids inside those gaps become larger with smaller gap distance as indicated by Eq. (1), which enhances the liquid–solid adhesion as observed by de Boer et al. (2000), Leseman et al. (2007) and (Raccurt et al., 2004). For "dry" contact, the real solid–solid adhesion $\gamma'_s \propto g_e / H_{avg}^2$ (Delrio et al., 2005). H_{avg} is the averaged gap distance of two rough surfaces and g_e is a function of H_{avg}, which describes the transition between the normal and retarded vdW forces. γ'_s increases monotonically with the decrease of H_{avg} as shown in Delrio's (2005) Fig. 4. Furthermore, when H_{avg} is very small, a phenomenon called capillary condensation (Wei and Zhao, 2007) can occur, which adsorbs the water molecules in the ambient air near the asperities and thus introduces/enhances the liquid–solid adhesion. Larger plastic and elastic deformations due to larger external load, which enhance both liquid–solid and solid–solid adhesion, are the mechanism responsible for the load history dependent property of adhesion measurement. As indicated in Eq. (20), even very small σ_d is sufficient to reduce the adhesion to a very small fraction of its value for smooth surfaces (Fuller and Tabor, 1975; Zhao et al., 2003), which should be a major reason causing the huge difference of adhesion measurement as listed in Table 1.

4. Summary

Some of the previous different or even contradicting experimental observations on MEMS stiction are discussed. A contact mechanics model, which probes the MEMS stiction from a different angle, is presented to explain different experimental observations and resolve some disputations. The model reveals that the stiction shape depends on the gap distance, beam span/stiffness, substrate mechanical properties and adhesion energy, etc. There is no need to assume the arc-shaped or the S-shaped deformation for a stuck beam, which may cause erroneous explanation of the experimental data. To explain the load history dependent property and large

experimental data difference of adhesion measurement, the surface topography of MEMS structures must be considered. Both the liquid–solid and solid–solid adhesions can be significantly enhanced by a larger external load, which is responsible for the loading history dependence of adhesion measurement observed in many experiments.

Appendix A. Arc-shaped and S-shaped deformations

Fig. 13 shows the arc-shape and S-shaped deformations and the coordinate system. When the beam is in stiction of no external load, the following governing equation holds:

$$w_{\xi\xi\xi\xi} = 0 \tag{22}$$

The solution to the above equation is

$$w(\xi) = A\xi^3 + B\xi^2 + C\xi + D \tag{23}$$

A, B, C and D are the four unknown constants to be determined by the boundary conditions.

For the arc-shaped beam, the following boundary conditions hold:

$$w(0) = 0, \quad w_\xi(0) = 0, \quad w(s_{arc}) = h, \quad w_{\xi\xi}(s_{arc}) = 0 \tag{24}$$

$w(\xi)$ of the arc-shaped beam is then solved as follows

$$w(\xi) = -\frac{h}{2s_{arc}^3}\xi^3 + \frac{3h}{2s_{arc}^2}\xi^2 \tag{25}$$

The (dimensional) suspension length of the arc-shaped beam is given by Eq. (3) (Yang, 2004)

$$S_{arc}^4 = \frac{3}{8}\frac{E_1 H^2 T^3}{\gamma_s} = \frac{9E_1 I H^2}{4B\gamma_s} \tag{26}$$
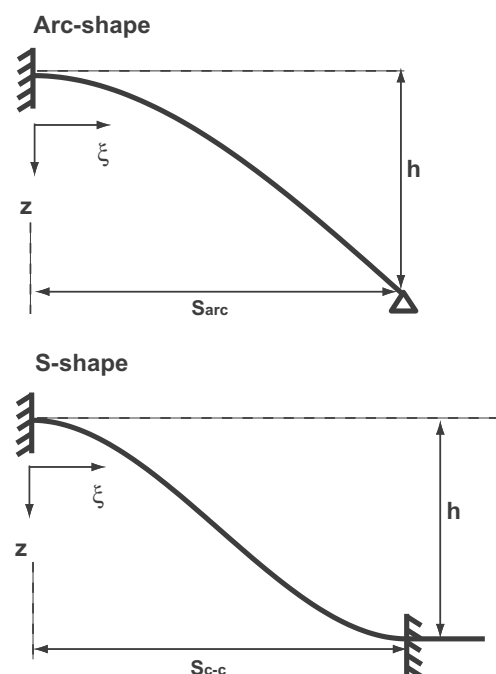

Fig. 13. Schematics of the arc-shaped and S-shaped beams.

According to the nondimensionalization scheme of Eq. (11), we have $s_{arc} = \beta S_{arc} = \sqrt[4]{9h^2/\alpha}$. Yang (2004) argued that at $\xi = s_{arc}$ the bending moment cannot be zero and the boundary conditions at $\xi = s_{arc}$ can only be the clamped one. Yang (2004) actually obtained the above suspension length of the arc-shaped beam by using the following different boundary conditions

$$w(0) = 0, \quad w_{\xi\xi}(0) = 0, \quad w(s_{arc}) = h, \quad w_{\xi}(s_{arc}) = 0 \tag{27}$$

For the S-shaped beam, the following boundary conditions hold:

$$w(0) = 0, \quad w_{\xi}(0) = 0, \quad w(s_{c-c}) = h, \quad w_{\xi}(s_{c-c}) = 0 \tag{28}$$

$w(\xi)$ of the S-shaped beam is solved as follows

$$w(\xi) = -\frac{2h}{s_{c-c}^3}\xi^3 + \frac{3h}{s_{c-c}^2}\xi^2 \tag{29}$$

The (dimensional) suspension length of the S-shaped beam is given by Eq. (3) (Yang, 2004)

$$S_{c-c}^4 = \frac{3}{2}\frac{E_1 H^2 T^3}{\gamma_s} = \frac{9 E_1 I H^2}{B \gamma_s} \tag{30}$$

The dimensionless $s_{c-c} = \beta S_{c-c} = \sqrt[4]{36h^2/\alpha}$ and $s_{arc} = \frac{\sqrt{2}}{2}s_{c-c}$. Eqs. (25) and (29) are also presented by de Boer et al. (1999).

Appendix B. Minimization of system total energy

U_B is the C–C beam bending energy, which has the following form:

$$
\begin{aligned}
U_B &= \frac{E_1 I}{2}\int_{-L_1}^{L_2}\frac{d^2 W}{dx^2}dx \\
&= \frac{E_1 I}{2}\left(\int_{-L_1}^{x_1}\frac{d^2 W_1}{dx^2}dx + \int_{x_1}^{x_2}\frac{d^2 W_2}{dx^2}dx + \int_{x_2}^{L_2}\frac{d^2 W_3}{dx^2}dx\right) \\
&= \frac{E_1 I \beta}{2}\left(\int_{-l_1}^{\xi_1}w_{1\xi\xi}^2 d\xi + \int_{\xi_1}^{\xi_2}w_{2\xi\xi}^2 d\xi + \int_{\xi_2}^{l_2}w_{3\xi\xi}^2 d\xi\right)
\end{aligned} \tag{31}
$$

In this paper, the concentrated load is at the beam center and distributed load is uniform, U_B can also be written as the following due to symmetry as if there are two cantilevers in contact with a substrate (Yang, 2004)

$$U_B = E_1 I \beta\left(\int_{-l_1}^{\xi_1}w_{1\xi\xi}^2 d\xi + \int_{\xi_1}^{0}w_{2\xi\xi}^2 d\xi\right) \tag{32}$$

For the arc-shaped beam deformation, because the contact is a point (i.e., $\xi_1 = 0$ and thus $\int_{\xi_1}^{0}w_{2\xi\xi}^2 d\xi = 0$), the contact part has no contribution to the bending energy; for the S-shaped beam deformation, because the contact part is (assumed to be) flat, i.e., w_2 is constant and $w_{2\xi\xi} = 0$, the contact part also has no contribution to the bending energy. As shown in Figs. 2 and 8, the contact zone is with a finite length and the beam deformation inside is not flat. Therefore, the bending energy inside contact zone in general should not be ignored.

The energy stored by the elastic foundation, U_F, is given as follows

$$U_F = \frac{k}{2}\int_{x_1}^{x_2}(W_2 - H)^2 dx = \frac{k}{2\beta^3}\int_{\xi_1}^{\xi_2}(w_2 - h)^2 d\xi \tag{33}$$

Again, both the arc-shaped and S-shaped deformations do not account this energy. That the arc-shaped and S-shaped deformations do not account the energy stored by the elastic foundation and the bending energy inside the contact zone is a major reason responsible for the difference between my beam deformation shape and arc-shape (or S-shape). The total elastic energy is $U_E = U_B + U_F$. In comparison, the bending energy inside the contact zone and U_F are not accounted by the energy approach (Legtenberg et al.,

1994; Mastrangelo and Hsu, 1993b; Raccurt et al., 2004; Yang, 2004) and by the fracture mechanics approach (de Boer and Michalske, 1999; de Boer et al., 1999; Knapp and de Boer, 2002; Jones et al., 2003a; Leseman et al., 2007).

The surface energy, U_S, is given as the following (Legtenberg et al., 1994; Mastrangelo and Hsu, 1993b; Yang, 2004)

$$U_S = -2B\gamma_s(x_2 - x_1) = -2B\gamma_s\beta^{-1}(\xi_2 - \xi_1) \tag{34}$$

$2B$ is the beam width and $x_2 - x_1 = 2A$ is the beam contact length. It is noticed that U_S is negative. Physically, the negative U_S means that when two surfaces unite to form an interface, the net free energy of the system reduces (Yu and Suo, 1998). It is this negative U_S that causes stiction.

The total free energy of the system is $U_T = U_E + U_S$ (Johnson, 1985; Legtenberg et al., 1994; Mastrangelo and Hsu, 1993b; Yang, 2004). For equilibrium, $\partial U_T/\partial\xi_1$ and $\partial U_T/\partial\xi_2$ vanish giving (Johnson, 1985; Legtenberg et al., 1994; Mastrangelo and Hsu, 1993b; Yang, 2004)

$$
\begin{aligned}
\frac{\partial U_T}{\partial\xi_1} &= -4[w_2(\xi_1) - h]^2 + \alpha = 0, \\
\frac{\partial U_T}{\partial\xi_2} &= -4[w_2(\xi_2) - h]^2 + \alpha = 0
\end{aligned} \tag{35}
$$

The dimensionless parameter α is defined in Eq. (19) as $\alpha = 4B\gamma_s/(E_1 I\beta^2) \approx 17.67\gamma_s/[T(E_2^2 E_1)^{1/3}]$. α indicates the adhesion influence in comparison of the elastic one between the beam and substrate. The derivation of $\partial U_T/\partial\xi_1$ and $\partial U_T/\partial\xi_2$ is lengthy, which is not expanded in full details. However, if some properties such as the following are applied, the derivation can be greatly simplified

$$\frac{\partial}{\partial\xi_1}\left[\int_{-l_1}^{\xi_1}w_{1\xi\xi}^2 d\xi\right] = w_{1\xi\xi}^2(\xi_1), \quad \frac{\partial}{\partial\xi_1}\left[\int_{\xi_1}^{\xi_2}w_{2\xi\xi}^2 d\xi\right]$$
$$= -w_{2\xi\xi}^2(\xi_1), \quad w_{1\xi\xi}(\xi_1) = w_{2\xi\xi}(\xi_1) \tag{36}$$

From Eq. (35), we have

$$w_2(\xi_1) = h \pm \frac{\sqrt{\alpha}}{2}, \quad w_2(\xi_2) = h \pm \frac{\sqrt{\alpha}}{2} \tag{37}$$

If $w_2(\xi_1) = w_2(\xi_2) = h + \frac{\sqrt{\alpha}}{2}$, physically it is the so-called sink-in phenomenon, which is frequently encountered in the indentation test (Zhang, 2010). The elastic foundation used in our model does not allow such phenomenon to occurs (Zhang, 2010). Therefore, $w_2(\xi_1)$ and $w_2(\xi_2)$ can only take the following forms

$$w_2(\xi_1) = h - \frac{\sqrt{\alpha}}{2}, \quad w_2(\xi_2) = h - \frac{\sqrt{\alpha}}{2} \tag{38}$$

From a fracture mechanics viewpoint on the MEMS stiction, $\sqrt{\alpha}/2$ is the critical normal crack opening displacement (Zhang, 2010). For asymmetric loading, $-\xi_1 \neq \xi_2$; for symmetric loading $-\xi_1 = \xi_2 = a$ ($a = \beta A$ is the dimensionless half contact length). Yang (2004) minimized his total energy by taking $\partial U_T/\partial a = 0$. Clearly, for symmetric loading, $\partial U_T/\partial a = -\partial U_T/\partial\xi_1 = \partial U_T/\partial\xi_2 = 0$. Minimizing the total system energy by requiring $\partial U_T/\partial a = 0$ can only be valid for symmetric loading scenario; $\partial U_T/\partial\xi_1 = 0$ and $\partial U_T/\partial\xi_2 = 0$ are capable of handling both asymmetric and symmetric loading scenarios.

References

Biot, M.A., 1937. Bending of an infinite beam on an elastic foundation. J. Appl. Mech. 4, 1–7.

de Boer, M.P., Michalske, T.A., 1999. Accurate method for determining adhesion of cantilever beams. J. Appl. Phys. 86, 817–827.

de Boer, M.P., Knapp, J.A., Mayer, T.M., Michalske, T.A., 1999. The role of interfacial properties on MEMS performance and reliability. Proc. SPIE 3825, 2–15.

de Boer, M.P., Knapp, J.A., Mayer, T.M., Michalske, T.A., 2000. Adhesion hysteresis of silane coated microcantilevers. Acta Mater. 48, 4531–4541.

Delrio, F., de Boer, M.P., Knapps, J.A., Reedy Jr., E., Clews, P., Dunn, M., 2005. The role of van der Waals forces in adhesion of micomachined surfaces. Nature Mater. 4, 629–634.

Evans, A.A., Lauga, E., 2009. Adhesion transition of flexible sheets. Phys. Rev. E 79, 066116.

Fuller, K.N.G., Tabor, D., 1975. The surface roughness on the adhesion of elastic solids. Proc. R. Soc. Lond. A 345, 327–342.

Ghatak, A., Mahadevan, L., Chaudhury, M.K., 2005. Measuring the work of adhesion between a soft confined film and a flexible plate. Langmuir 21, 1277–1281.

Giri, M., Bousfield, D.B., Unertl, W.N., 2001. Dynamic contacts on viscoelastic film: work of adhesion. Langmuir 17, 2973–2981.

Gladwell, G.M., 1976. On some unbonded contact problems in plane elasticity theory. J. Appl. Mech. 43, 263–267.

Greenwood, J.A., Williamson, J.B.P., 1966. Contact of nominally flat surfaces. Proc. R. Soc. Lond. A 295, 300–318.

Greenwood, J.A., Tripp, J.H., 1967. The elastic contact of rough spheres. J. Appl. Mech. 34, 153–159.

Hariri, A., Zu, J.W., Ben Mrad, R., 2006. Modeling of dry stiction in micro-electro-mechanical systems (MEMS). J. Micromech. Microeng. 16, 1195–1206.

Johnson, K.L., 1985. Contact Mechanics. Cambridge University Press, Cambridge.

Jones, E.E., Begley, M.R., Murphy, K.D., 2003a. Adhesion of micro-cantilever subjected to mechanical point loading: modeling and experiments. J. Mech. Phys. Solids 51, 1601–1622.

Jones, E.E., Murphy, K.D., Begley, M.R., 2003b. Mechanical measurements of adhesion in microcantilevers: transitions in geometry and cyclic energy changes. Exp. Mech. 43, 280–288.

Kerr, A.D., 1976. On the derivation of well posed boundary value problems in structural mechanics. Int. J. Solids Struct. 12, 1–11.

Kerr, A.D., 1979. On the unbonded contact between elastic and elastic–rigid media. Acta Mech. 33, 135–146.

Knapp, J.A., de Boer, M.P., 2002. Mechanics of microcantilever beams subjected to combined electrostatic and adhesive forces. J. Microelectromech. Syst. 11, 754–764.

Legtenberg, R., Tilmans, T., Elders, J., Elwenspoek, M., 1994. Stiction of surface micromachined structures after rinsing and drying: model and investigation of adhesion mechanisms. Sens. Actuators A 43, 230–238.

Leseman, Z.C., Carlson, S.P., Mackin, T.J., 2007. Experimental measurements of the strain energy release rate for stiction-failed microcantilevers using a single-cantilever beam peel test. J. Microelectromech. Syst. 16, 38–43.

Liu, J.L., 2010. Theoretical analysis on capillary adhesion of microsized plates with a substrate. Acta Mech. Sin. 26, 217–223.

Mastrangelo, C.H., Hsu, C.H., 1993a. Mechanical stability and adhesion of microstructures under capillary forces—part I: basic theory. J. Microelectromech. Syst. 2, 33–43.

Mastrangelo, C.H., Hsu, C.H., 1993b. Mechanical stability and adhesion of microstructures under capillary forces—part II: experiments. J. Microelectromech. Syst. 2, 44–55.

Miller, R.E., Shenoy, V.B., 2000. Size-dependent elastic properties of nanosized structural elements. Nanotechnology 11, 139–147.

Press, W.H., Teukolsky, S.A., Vetterling, W.T., Flannery, B.P., 1992. Numerical Recipes in Fortran, second ed. Cambridge University Press, Cambridge (Chapter 9).

Raccurt, O., Tardif, F., d'Avitaya, F., Vareine, T., 2004. Influence of liquid surface tension on stiction of SOI MEMS. J. Micromech. Microeng. 14, 1083–1090.

Roark, R.J., 1954. Formulas for Stress and Strain, third ed. McGrall-Hill Book Company, New York (Chapter 8).

Rogers, J.W., Mackin, T.J., Phinney, L.M., 2002. A thermomechanical model for adhesion reduction of MEMS cantilevers. J. Microelectromech. Syst. 11, 512–520.

Savkar, A., Murphy, K.D., Leseman, Z.C., Mackin, T.J., Begley, M.R., 2007. On the use of structural vibrations to release stiction failed MEMS. J. Microelectromech. Syst. 16, 163–173.

Sun, Y., Akhremitchev, B., Walker, G.C., 2004. Using the adhesive interaction between atomic force microscopy tips and polymer surfaces to measure the elastic modulus of compliant sample. Langmuir 20, 5837–5845.

Tas, N.R., Gui, C., Elwenspoek, M., 2003. Static friction in elastic adhesion contacts in MEMS. J. Adhes. Sci. Tech. 17, 547–561.

Tian, X., Bhushan, B., 1996. The micro-meniscus effect of a thin liquid film on the static friction of rough surface contact. J. Phys. D: Appl. Phys. 29, 163–178.

Timoshenko, S., 1956. Strength of Materials: II. Advanced Theory and Problems, third ed. Van Nostrand, New York, p. 71.

van Spengen, W.M., Puers, R., De Wolf, I., 2002. A physical model to predict stiction in MEMS. J. Micromech. Microeng. 12, 702–713.

Wei, Z., Zhao, Y.P., 2007. Growth of liquid bridge in AFM. J. Phys. D: Appl. Phys. 40, 4368–4375.

Weitsman, Y., 1970. On foundations that reacts in compression only. J. Appl. Mech. 37, 1019–1030.

Wong, M.F., Duan, G., Wan, K.T., 2007. Adhesion-delamination mechanics of a prestressed rectangular film adhered onto a rigid substrate. J. Appl. Phys. 101, 024903.

Yang, F., 2004. Contact deformation of a micromechanical structure. J. Micromech. Microeng. 14, 263–268.

Yu, H.H., Suo, Z., 1998. A model of wafer bonding by elastic accommodation. J. Mech. Phys. Solids 46, 829–844.

Zhang, Y., 2008a. Tensionless contact of a finite beam resting on Reissner foundation. Int. J. Mech. Sci. 50, 1035–1041.

Zhang, Y., 2008b. Transitions between different contact models. J. Adhes. Sci. Tech. 22, 699–715.

Zhang, Y., 2010. Extracting nanobelt mechanical properties from nanoindentation. J. Appl. Phys. 107, 123518.

Zhang, Y., Murphy, K.D., 2004. Response of a finite beam in contact with a tensionless foundation under symmetric and asymmetric loading. Int. J. Solids Struct. 41, 6745–6758.

Zhang, Y., Zhao, Y.P., 2004. Static study of cantilever beam stiction and electrostatic force influence. Acta Mech. Solida Sin. 17, 104–112.

Zhang, Y., Zhao, Y.P., 2005. Vibration of an adhered microbeam under a periodically shaking electrical force. J. Adhes. Sci. Tech. 19, 799–815.

Zhang, Y., Zhao, Y.P., 2006. Numerical and analytical study on the pull-in instability of micro-structure under electrostatic loading. Sens. Actuators A 127, 366–380.

Zhang, Y., Zhao, Y.P., 2011. A precise model for the shape of an adhered microcantilever. Sens. Actuators A 171, 381–390.

Zhao, Y.P., Wang, L.S., Yu, T.X., 2003. Mechanics of adhesion in MEMS—a review. J. Adhes. Sci. Tech. 17, 519–546.